Annals of Biomedical Engineering, Vol. 26, pp. 166–178, 1998
Printed in the USA. All rights reserved.

0090-6964/98 $10.50 + .00

A Mathematical Model of Gas Exchange in an Intravenous Membrane Oxygenator

TODD J. HEWITT,* BRACK G. HATTLER,† and WILLIAM J. FEDERSPIEL*†‡

*Bioengineering Program, †Artificial Lung Program, Department of Surgery, and ‡the Department of Chemical Engineering, University of Pittsburgh, Pittsburgh, PA

(Received 26 December 1996; accepted 31 July 1997)

Abstract—Acute respiratory distress syndrome (ARDS) is a pulmonary edemic condition which reduces respiratory exchange in 150,000 people per year in the United States. The currently available therapies of mechanical ventilation and extracorporeal membrane oxygenation are associated with high mortality rates, so intravenous oxygenation represents an attractive, alternative support modality. We are developing an intravenous membrane oxygenator (IMO) device intended to provide 50% of basal oxygen and carbon dioxide exchange requirements for ARDS patients. A unique aspect of the IMO is its use of an integral balloon to provide active mixing. This paper describes a mathematical model which was developed to quantify and optimize the gas exchange performance of the IMO. The model focuses on balloon activated mixing, uses a lumped compartment approach, and approximates the blood-side mass transfer coefficients with cross-flow correlations. IMO gas exchange was simulated in water and blood, for a variety of device geometries and balloon pulsation rates. The modeling predicts the following: (1) gas exchange efficiency is reduced by a buildup of oxygen in the fluid near the fibers; (2) the IMO gas exchange rate in blood is normally about twice that in water under comparable conditions; (3) a balloon diameter of about 1.5 cm leads to optimal gas exchange performance; and (4) *in vivo* positioning can affect gas exchange rates. The numerically predicted gas transfer rates correlate closely with those experimentally measured *in vitro* for current IMO prototypes. © *1998 Biomedical Engineering Society.* [S0090-6964(98)00602-X]

Keywords—ARDS, Intravenous oxygenation, Artificial lung, Mathematical model.

INTRODUCTION

Acute respiratory distress syndrome (ARDS) refers to reversible, noncardiogenic pulmonary edema arising from a variety of different insults to the lung tissue. The disease affects approximately 150,000 people per year in the United States[3] and treatment requires respiratory support using conventional therapies of mechanical ventilation, and/or extracorporeal membrane oxygenation (ECMO) for patients with severe ARDS. The positive airway pressures and volume excursions associated with mechanical ventilation can result in further damage to lung tissue, including barotrauma (high airway pressures), volutrauma (lung distension) and parenchymal damage from the toxic levels of oxygen required for effective mechanical ventilation.[19] The alternative use of ECMO is complicated and expensive, requiring extensive blood/biomaterial contact in extracorporeal circuits, systemic anticoagulation, and labor-intensive patient monitoring. Due to these complications, the mortality rate of ARDS patients remains high, exceeding 50% in adults.[6,7,15,16]

Intravascular oxygenation represents an attractive, alternative support modality for patients with ARDS. The concept of intravascular oxygenation as an alternative ARDS therapy originated with Mortensen,[13] who developed an intravenous oxygenator (IVOX) consisting of a bundle of crimped hollow fibers which was positioned in the vena cava. In phase I clinical trials, the IVOX provided an average of 28% of basal gas exchange requirements for patients with severe ARDS.[2] The clinical study, however, concluded that more gas exchange was needed for intravascular oxygenation to be clinically effective in ARDS treatment. We are developing an intravenous membrane oxygenator (IMO) with a design goal of 50% of basal oxygen and carbon dioxide exchange requirements for end-stage ARDS patients. Like the IVOX, the IMO consists of a bundle of manifolded hollow fibers, and is intended for intravenous placement within the superior and inferior vena cavae (Fig. 1). The target level of gas exchange in the IMO, however, is almost twice that achieved with the IVOX, and consequently, the IMO incorporates a polyurethane balloon concentric with the fiber bundle, which rhythmically inflates and deflates to provide active blood mixing, and thus enhances gas exchange. Our current efforts focus on device improvements intended to provide the target levels of gas exchange, given the constraints imposed by intravenous placement on fiber bundle size and hence

Address for all correspondence: William J. Federspiel, Ph.D., Artificial Lung Program, University of Pittsburgh, Room 428, Biotechnology Center, Pittsburgh, PA 15219. Electronic mail: Federspiel@pittsurg.nb.upmc.edu

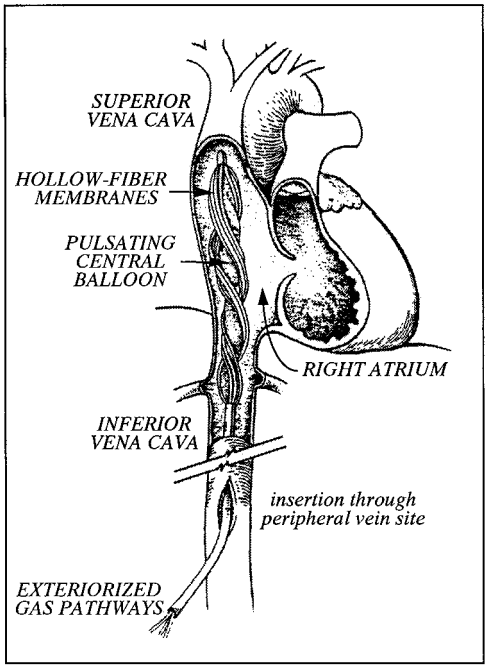

FIGURE 1. *In situ* placement of the IMO.

fiber surface area for gas exchange. We expect that a maximum of 0.5 m^2 of fiber surface area can be placed within the vena cava without obstructing venous return.[13]

This paper describes a mathematical design model for the IMO, which can be used to predict and optimize the oxygen exchange performance of the device. While CO_2 exchange is also important, our *in vivo* studies[10] indicate that O_2 exchange rates in the IMO are less than those for CO_2, indicating that O_2 transfer is the limiting factor. The use of similar design models for intracorporeal oxygenators has been explored by Niranjan *et al.*[14] and Makarewicz.[11] Niranjan *et al.* developed a model for the IVOX device, which focuses on individual fibers, treating them as noninteracting, cylindrical repeating units, each surrounded by an attendant annular sleeve of blood of arbitrarily defined size. This approach assumes parallel flow past the fibers, and is similar to the Krogh cylinder model for capillary oxygen exchange. Makarewicz developed a numerical procedure for approximating mass transfer in both intravascular and extracorporeal artificial lungs. This scheme divides the oxygenator into a discrete number of fiber rows, with each individual fiber oriented in cross flow to the blood. While both these approaches provide valuable insight into gas exchange in static intravascular artificial lungs, neither is applicable to the IMO, which uses a pulsating balloon to drive flow through the fiber bundle. The use of a pulsating balloon subjects the IMO to a different set of geometric and operational considerations. For instance, balloon size is an optimizable geometric parameter. A small balloon will engender little mixing, and thus the gas exchange efficiency of the device will be poor. Conversely, a large balloon will detract from the space available for fibers. Furthermore, since gas transfer is facilitated largely by balloon motion, the dynamics of balloon inflation (e.g., the inflation–deflation temporal wave form) may directly influence gas exchange efficiency. Clearly, an IMO design model that elucidates the interplay between geometry, dynamics, and gas transfer can aid in the development of a more effective intravenous oxygenator.

METHODS

Geometry of the Design Model

The intravenous membrane oxygenator is idealized as three interacting, lumped compartments; the shunt, fiber, and balloon space regions, as shown in cross-sectional and longitudinal views in Fig. 2(a) and 2(b). The outermost shunt region consists of the annular space between the outside of the fiber bundle and the inner vessel wall, which gains volume with balloon inflation so as to accommodate the displaced fluid. The region between the outside of the balloon and the inside of the fiber region is the balloon space volume, which also varies with time as the balloon inflates and deflates. The fluid in the annular, fiber-packed, time-independent volume surrounding the balloon space constitutes the fiber region. The geometry is assumed to be cylindrical and axisymmetric [Fig. 2(a)], and varies with time as the balloon inflates and deflates (except for the fiber compartment, which has a constant volume).

Communication between the compartments occurs solely by convective flow, as summarized in Fig. 2(c). Fluid moving down the axis of the vessel flows into the shunt volume around the device (since it cannot flow directly into the fiber bundle). This fluid is delivered to the shunt compartment at a longitudinal flow rate Q_L and a venous PO_2, P_{in}. Balloon deflation generates a flow rate $Q_b(t)$, which draws this shunt fluid into the fiber and balloon space regions, where its PO_2 increases to $P_F(t)$ in the fiber region and $P_{\text{bs}}(t)$ in the balloon space compartment due to gas exchange with the fibers. With balloon inflation, the oxygenated fluid moves back into the shunt volume and mixes with the existing shunt fluid. Meanwhile, fluid leaves the shunt volume at the same longitudinal flow rate, Q_L, with which it is delivered, but at a higher PO_2, $P_s(t)$.

Transport Equations

The governing differential equations are derived from oxygen mass balances on each of the compartments. During inflation, the fiber region gains oxygen by convection from the balloon volume and diffusion from the

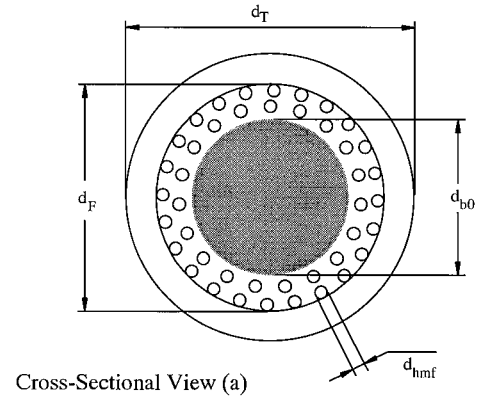

Cross-Sectional View (a)

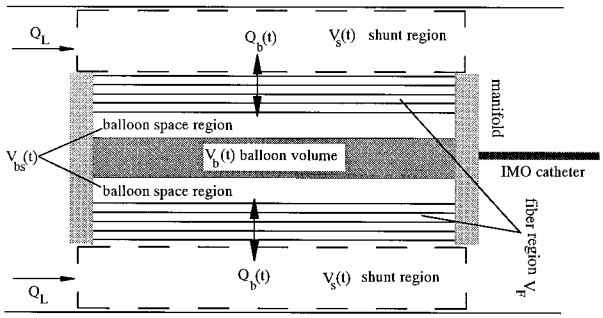

Longitudinal View (b)

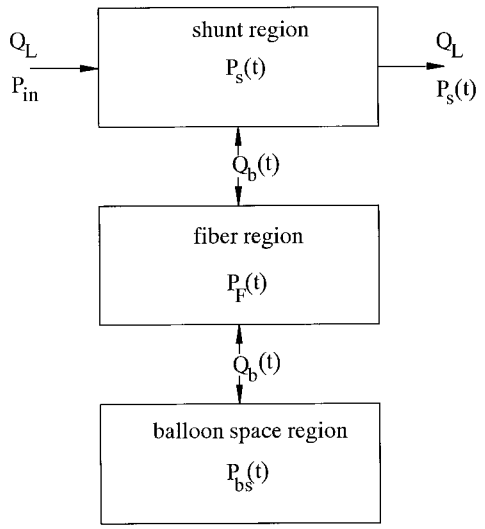

(c) Box Diagram

FIGURE 2. (a) Cross sectional, (b) longitudinal, and (c) box diagram views of the idealized IMO. d_T is the tube or vessel diameter (depending upon whether the device is *in vitro* or *in vivo*), d_F is the overall device diameter, d_{b0} is the balloon diameter at full inflation, and d_{hmf} is the outer diameter of an individual fiber. Q_L is the longitudinal fluid flow rate, $V_b(t)$ and $Q_b(t)$ are the balloon volume and flow rate, respectively. $V_{bs}(t)$, V_F, and $V_s(t)$ are the volumes of the balloon space, fiber region, and shunt volumes, respectively. Likewise, $P_{bs}(t)$, $P_F(t)$, and $P_s(t)$ are the PO_2 values of the balloon space, fiber region, and shunt volumes, respectively.

fibers, but loses O_2 by convection to the shunt compartment. The net rate of O_2 accumulation in the fiber region during inflation is therefore

$$\frac{d}{dt}\{\alpha(P)V_F P_F(t)\} = KA\{\overline{P_{if}} - P_F(t)\} - \alpha(P)|Q_b(t)|P_F(t) + \alpha(P)|Q_b(t)|P_{bs}(t), \quad (1)$$

where $P_F(t)$ and V_F are the O_2 partial pressure and the volume of fluid in the fiber region, respectively, $Q_b(t)$ is the balloon flow rate, K represents the mass transfer coefficient (or permeability) of oxygen diffusing from the fibers, A is the device area, $\overline{P_{if}}$ is the average intrafiber pressure, $\alpha(P)$ is the effective oxygen solubility of the fluid as defined below in Eqs. (7) and (8), and $P_{bs}(t)$ is the PO_2 in the balloon space region. During deflation, oxygen is convected into the fiber region from the shunt region and convected out into the balloon space volume. Hence,

$$\frac{d}{dt}\{\alpha(P)V_F P_F(t)\} = KA\{\overline{P_{if}} - P_F(t)\} + \alpha(P)|Q_b(t)|P_s(t) - \alpha(P)|Q_b(t)|P_F(t), \quad (2)$$

where $P_s(t)$ represents the PO_2 within the shunt compartment.

The shunt volume simultaneously receives and loses oxygen due to the longitudinal flow rate Q_L, regardless of balloon motion. During inflation, the shunt compartment also gains oxygen from the fiber region:

$$\frac{d}{dt}\{\alpha(P)V_S(t)P_S(t)\} = \alpha(P)Q_L P_{in} - \alpha(P)Q_L P_s(t) + \alpha(P)|Q_b(t)|P_F(t), \quad (3)$$

where $V_s(t)$ is the volume of the shunt compartment and P_{in} is the inlet (venous) PO_2. Conversely, O_2 is convected out of the shunt region into the fiber region during deflation:

$$\frac{d}{dt}\{\alpha(P)V_S(t)P_S(t)\} = \alpha(P)Q_L P_{in} - \alpha(P)Q_L P_s(t) - \alpha(P)|Q_b(t)|P_S(t). \quad (4)$$

Finally, the balloon space volume loses O_2 to the fiber region during inflation:

$$\frac{d}{dt}\{\alpha(P)V_{\mathrm{bs}}(t)P_{\mathrm{bs}}(t)\} = -\alpha(P)|Q_b(t)|P_{\mathrm{bs}}(t), \quad (5)$$

and gains O_2 from the fiber region during deflation:

$$\frac{d}{dt}\{\alpha(P)V_{\mathrm{bs}}(t)P_{\mathrm{bs}}(t)\} = \alpha(P)|Q_b(t)|P_F(t), \quad (6)$$

where $V_{\mathrm{bs}}(t)$ is the volume of the balloon space compartment.

Several assumptions have simplified this analysis. The PO_2 in a given compartment is considered uniform (e.g., there are no intracompartment spatial PO_2 variations). Similarly, the length-wise intrafiber PO_2 variations, which arise from the vacuum-driven flow of oxygen gas through the fiber lumens, are considered small enough that the intrafiber PO_2 at any point can be represented by a mean value P_{if}. For a gas flow of 3 L/min in our current prototypes, the intrafiber pressure drop is approximately 100 mm Hg, and P_{if} is therefore about 700 mm Hg. These assumptions make the equations more tractable than with the inclusion of spatial PO_2 variations, which would require solving the coupled Navier–Stokes and species-continuity equations. In addition, Lund[9] demonstrated that balloon movement in the IMO engenders significant fluid mixing, which would attenuate spatial variations (radial and axial). Finally, since this analysis focuses on balloon-engendered active mixing, movement of O_2 from one compartment to another is assumed to occur by convection only, with molecular diffusion being secondary. Diffusional exchange is important at the fiber surface, however, and is accounted for by the permeability or mass transfer coefficient (K).

We have introduced an effective solubility term, $\alpha(P)$, which makes the equations more compact. In water, solubility reflects simple dissolution only:

$$\alpha(P) = \alpha_{\mathrm{w}}, \quad (7)$$

where α_{w} is the solubility coefficient of oxygen in water. In blood, the total concentration of O_2, c_{Total}, is equal to the concentration of dissolved O_2 plus that bound to hemoglobin: $c_{\mathrm{Total}} = \alpha_{\mathrm{b}}PO_2 + c_T SO_2$, where α_{b} is the solubility of oxygen in blood, c_T is the binding capacity of hemoglobin, and SO_2 is the fractional saturation of hemoglobin. Factoring out the PO_2 leads to $c_{\mathrm{Total}} = PO_2(\alpha_{\mathrm{b}} + c_T SO_2/PO_2)$. The effective solubility for blood is therefore

$$\alpha(P) = \alpha_{\mathrm{b}} + c_T SO_2/PO_2. \quad (8)$$

This definition of effective solubility is unique to our application, since the governing Eqs. (1)–(6) are written with the effective solubility term inside the derivative (which makes the equations applicable to both blood and water). The oxyhemoglobin dissociation curve (SO_2 vs PO_2) is approximated using the Hill equation (all results in this paper are for bovine blood).[11]

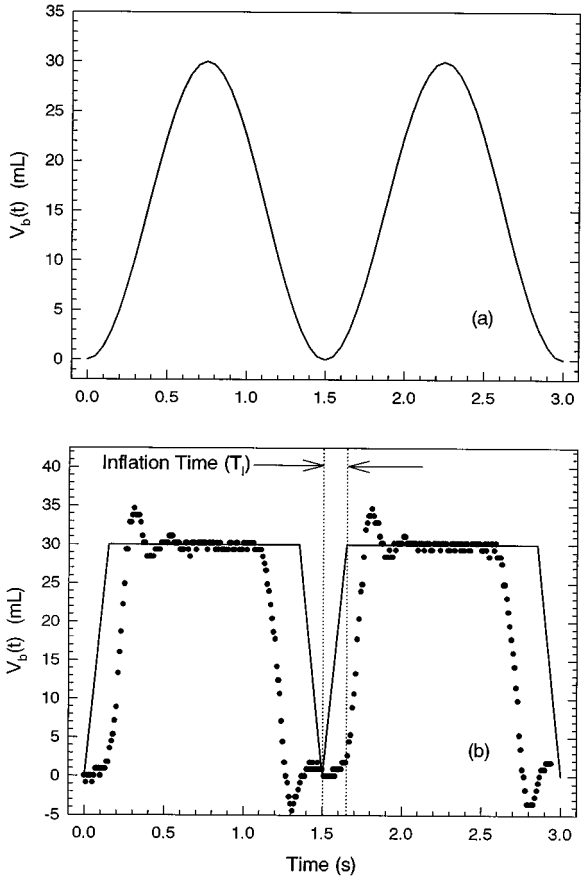

FIGURE 3. Balloon volume vs time for (a) sinusoidal inflation and (b) impulsive inflation. The solid line in (b) is the mathematical approximation used in the model [Eq. (12)] and the points are actual data [(a) is Eq. (10)]. The balloon volume is 30 mL, and the ±5 mL "spikes" seen in the acquired data are artifacts of the measurement apparatus.

Balloon and Compartment Dynamics

Balloon inflation and deflation is modeled for two different modes of pulsation [Figs. 3(a) and 3(b)]. The first balloon pulsation mode is sinusoidal inflation, where balloon volume $V_b(t)$ varies as

$$V_b(t) = \frac{V_0}{2}(1 - \cos 2\pi f t), \quad (9)$$

and hence the convective flow, $Q_b(t) = dV_b/dt$, generated by the balloon is

$$Q_b(t) = \pi f V_0 \sin 2\pi f t, \quad (10)$$

where V_0 is the volume of the balloon when fully inflated and f is the frequency of pulsation.

The second mode of balloon pulsation is impulsive inflation [Fig. 3(b)]. Shown in Fig. 3(b) are the actual and theoretical balloon volume versus time profiles. The data were obtained using a plethysmographic technique as previously described,[4] where the IMO is submerged in an airtight, partially water-filled chamber. Balloon inflation causes the water level to rise, compressing the volume of gas at the top of the chamber and therefore increasing the pressure. These pressure changes are recorded with pressure transducers and converted into volume excursions using the Ideal Gas Law. As seen in Fig. 3(b), the impulsive inflation model more closely approximates the actual behavior of the Datascope Intra-Aortic Balloon Pump (IABP) System 90 console, which is currently used to drive balloon pulsation. In the impulsive mode, the balloon takes a fixed amount of time, T_I, to inflate or deflate, regardless of frequency,

$$V_b(t)=\begin{cases} V_0 t/T_I, & 0<t\leq T_I, \\ V_0, & T_I<t\leq T-T_I, \\ V_0(T-t)/T_I, & T-T_I<t\leq T. \end{cases} \quad (11)$$

The balloon-generated flow rate is obtained by taking the derivative of Eq. (11)

$$Q_b(t)=\begin{cases} V_0/T_I, & 0<t\leq T_I, \\ 0, & T_I<t\leq T-T_I, \\ -V_0/T_I, & T-T_I<t\leq T. \end{cases} \quad (12)$$

The T_I parameter may be slightly different for different prototypes (due to different catheter delivery systems), but is relatively insensitive to frequency in a given prototype. Thus, increasing frequency decreases the time the balloon spends in its motionless, inflated state, but does not change the rapidity of balloon inflation or deflation.

The volumes of the compartments can be specified once the balloon dynamics are prescribed. The volume of the fiber region fluid is fixed with respect to time, and thus depends only on device geometry:

$$V_F=\frac{\pi}{4}(d_F^2-d_{b0}^2)L\epsilon, \quad (13)$$

where d_F is the overall device diameter, d_{b0} is the diameter of the balloon at full inflation, L is the device length, and ϵ is the fiber bundle porosity (fractional void volume). The volume of the balloon space, however, varies with time as the balloon inflates and deflates:

$$V_{\mathrm{bs}}(t)=V_0-V_b(t), \quad (14)$$

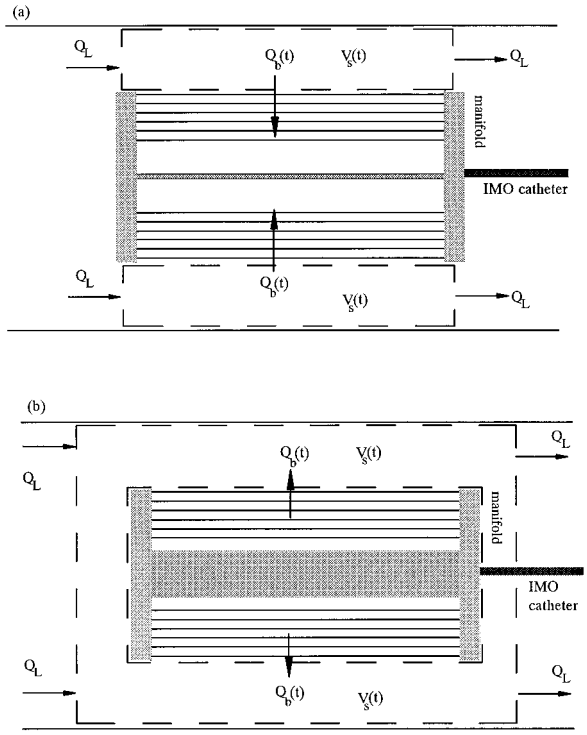

FIGURE 4. Shunt volume during (a) deflation and (b) inflation.

where V_0 is the volume of the balloon at full inflation $[V_0=(\pi/4)d_{b0}^2L]$. Note that the balloon space region consists of the volume of fluid outside the balloon, between the balloon surface and the fiber bundle, while the balloon volume is the amount of gas inside the balloon.

Figure 4 conceptually illustrates how the volume of the shunt compartment changes with time as the balloon inflates and deflates. The shunt volume expands and contracts as the balloon fills and empties:

$$V_s(t)=V_{s0}+V_b(t), \quad (15)$$

where V_{s0} is the volume of the shunt compartment when the balloon is deflated $[V_{s0}=(\pi/4)(d_T^2-d_F^2)L]$, and d_T is the diameter of the tube or vessel. The shunt compartment could have been modeled as a fixed control volume, with $V_s(t)=V_{s0}$. In this case, balloon motion would alter the longitudinal flow rate Q_L, possibly even causing it to become negative. Such an approach presents several challenges. First, it would be necessary to model the properties of the vessel wall, since vessel deformation (e.g., diametric expansion with balloon inflation) could lead to an additional, time-varying radial flow rate into and out of the shunt compartment. Second, two time-varying longitudinal flow rate terms would be needed, $Q_{L,\mathrm{in}}(t)$ and $Q_{L,\mathrm{out}}(t)$. Finally, some fluid might move upstream of the device with balloon inflation

[when $Q_{L,\text{in}}(t)<0$]. It would therefore be unclear what to use as the inlet PO_2 when the flow reversed direction [$Q_{L,\text{in}}(t)>0$] since some of the oxygenated fluid would mix with fluid not yet exposed to the device. The deforming control volume approach implemented in this analysis provides a more tractable method for modeling these phenomena. Since the shunt volume is allowed to expand longitudinally and/or radially, Q_L implicitly varies with time at a fixed point in space. During inflation, for instance, the shunt volume is expanding proximally and distally, thereby displacing fluid across the lines $x=0$ (proximal end) and $x=L$ (distal end). This is effectively the same as imposing oscillatory terms on both $Q_{L,\text{in}}$ and $Q_{L,\text{out}}$; e.g., $Q_{L,\text{in}}(t)=Q_L+\xi Q_b(t)$, where ξ represents the fraction of balloon-generated flow rate which is displaced proximally and $Q_{L,\text{in}}(t)$ is the flow rate at $x=0$. Similarly, the mixing of oxygenated and unoxygenated fluid with balloon motion is accounted for by the dilution of oxygen with shunt volume expansion (or increase in concentration with volume contraction). With a deforming control volume, however, Q_L and P_{in} remain constant since they represent conditions upstream and downstream of the device (e.g., in regions unaffected by balloon motion), and it is not necessary to guess a value for ξ. This approach assumes that shunt volume PO_2 remains spatially uniform during inflation/deflation, but this is a logical extension of the lumped compartment approach.

Mass Transfer Coefficient

The permeability, or mass transfer coefficient K, relates the O_2 exchange rate to the fiber surface area and the PO_2 differential between the fiber interior and the surrounding fluid:

$$\dot{V}_{O_2}=KA\Delta P, \tag{16}$$

where $\dot{V}_{O_2}$ is the oxygen transfer rate and ΔP is the driving force for transfer. The permeability K is determined from empirical mass transfer correlations for cross flow to fiber beds. These correlations are of the general form $\text{Sh}=a(\text{Re})^b\text{Sc}^{1/3}$, where $\text{Sh}=Kd/\alpha D$ (Sherwood number), $\text{Re}=Vd_h/\nu$ (Reynolds number), and $\text{Sc}=\nu/D$ (Schmidt number), with the characteristic length (hydraulic diameter), diffusivity, viscosity, and average velocity given by d_h, D, ν, and V, respectively.

Previous investigators[1,5,12,17,18,20,21] have studied mass transfer in steady-state flow situations for modules of packed hollow fibers, and determined correlations for a range of porosities, Reynolds numbers, and geometries for gas transfer to water and blood. We have also referenced one heat transfer correlation[8] for a cylinder in cross flow. Many of the correlations are developed for either very high or very low porosity devices. For instance, Yang and Cussler[21] develop cross-flow correlations for oxygen and carbon dioxide transfer in a 72 fiber module ($\epsilon=0.93$) and a 750 fiber module ($\epsilon=0.3$) in water, and the a and b values differ for the two correlations. The a and b values also depend upon how carefully made the fiber module is, and tend to be higher for handmade modules than for commercial oxygenators. We have decided to average the a and b values from previous experiments[1,5,8,17,18,20,21] in this analysis, for two reasons. First, we are interested in simulating devices with a range of porosity values ($\epsilon\approx 0.2$–0.7), which may be best characterized by intermediate a and b values. Similarly, the gas exchange coefficients for the IMO will likely fall between those for the most efficient handmade devices and the least efficient manufactured devices. Average a and b values were therefore obtained by plotting Sh vs Re over the relevant Reynolds number range (about 3–5 for blood and 12–15 for water) for each correlation, then averaging the curves together and determining a and b with nonlinear regression analysis. The values thus obtained were 0.524 and 0.523 for a and b, respectively. Since the a and b values are model input parameters, however, more IMO-specific simulations can be run in the future when more appropriate (e.g., porosity dependent) a and b values are determined.

The Reynolds number for cross flow in the IMO device is given by $\text{Re}=V_r d_h/\nu$, where V_r is the spatially averaged transverse velocity and d_h is the hydraulic diameter. For a packed fiber bundle, with $\epsilon<0.5$, the hydraulic diameter can be expressed in terms of the outer diameter of an individual fiber, d_{hmf}, and the fiber bundle porosity (ϵ): $d_h=d_{hmf}(\epsilon/(1-\epsilon))$. For a prototype with less densely packed fibers ($\epsilon>0.5$), the hydraulic diameter is more accurately described by d_{hmf}. The transverse velocity is obtained by dividing the balloon-generated flow rate, $Q_b(t)$, by the average area available for transverse flow, $A_r\epsilon$: $V_r(t)=Q_b(t)/A_r\epsilon$. The average area can be approximated by $A_r\epsilon\approx(\pi/2)(d_{b0}+d_F)L\epsilon$. While both transverse area and velocity depend on the radial coordinate, r (since area for flow increases as the fluid moves radially outward), we have found that including these variations does not significantly affect the results, and have therefore omitted them for simplicity. Combining all of these relations gives the permeability of oxygen in water as a function of the balloon-engendered flow rate, $Q_b(t)$:

$$K_{\text{w}}=a\alpha_{\text{w}}d_h^{(b-1)}D_{\text{w}}^{2/3}\nu_{\text{w}}^{(1/3-b)}\left(\frac{2Q_b(t)}{\pi(d_{b0}+d_F)L\epsilon}\right)^b, \tag{17}$$

where α_{w}, D_{w}, and ν_{w} are the solubility and diffusivity of oxygen in water, and the viscosity of water, respec-

TABLE 1. Physical constants.

Parameter	Description	Value
α_w	Solubility of oxygen in water	3.16×10^{-4} mL O_2 mL^{-1} cm Hg^{-1}
α_b	Solubility of oxygen in blood	3.0×10^{-4} mL O_2 mL^{-1} cm Hg^{-1}
D_w	Diffusivity of oxygen in water	2.8×10^{-5} cm^2 s^{-1}
D_b	Diffusivity of oxygen in blood	1.8×10^{-5} cm^2 s^{-1}
ν_w	Kinematic viscosity of water	7.0×10^{-3} cm^2 s^{-1}
ν_b	Kinematic viscosity of blood	2.35×10^{-2} cm^2 s^{-1}
c_T	Hemoglobin binding capacity of blood	0.167 mL O_2/mL blood
P_{in}(water)	Inlet PO_2 for water (*in vitro*)	20 mm Hg
P_{in}(blood)	Inlet (venous) PO_2 for blood (*in vivo*)	40 mm Hg
P_{if}	Average intrafiber pressure	700 mm Hg
Q_L	Longitudinal fluid flow rate	3 L/min

tively. Table 1 gives the values and units of all the relevant physical parameters.

This model simulates gas exchange engendered by the cross flow which arises from balloon pulsation. Hence, when the balloon is not oscillating $[Q_b(t)=0]$, the permeability is zero, and no mass transfer occurs. Experimentally, there is some mass transfer when the balloon is not moving due to longitudinal fluid convection within the fiber bundle, but this effect has not been considered here. Inclusion of gas exchange from longitudinal convection would complicate the model. Moreover, we are designing a device intended to drive fluid into and out of the fiber region predominantly by balloon pulsation (i.e., at 0 bpm, the fluid is shunted around the device completely), so as to minimize the flow resistance incurred by the device. Accordingly, mass transfer in the absence of balloon motion is secondary to that engendered by balloon pulsation.

Mass Transfer Coefficient for Blood

Vaslef *et al.*[18] suggested and validated a method for relating permeability coefficients in water to those in blood. While the relation $\mathrm{Sh}=a(\mathrm{Re})^b(\mathrm{Sc})^{1/3}$ applies to blood with the same a and b values, the solubility and diffusivity terms, α and D, must be interpreted appropriately for blood, given the hemoglobin binding characteristics of the erythrocytes. This leads to the definition of an ''effective diffusivity'' term, which combines the physical diffusivity of oxygen in blood (D_b) and the properties of hemoglobin,

$$D_{\mathrm{eff}}=\frac{D_b}{1+c_T\lambda(\mathrm{PO_2})/\alpha_b}, \tag{18}$$

where $\lambda(\mathrm{PO_2})$ is $d\mathrm{SO_2}/d\mathrm{PO_2}$. The Vaslef analysis indicates that the effective diffusivity is used in calculating the Schmidt number for blood, whereas the Sherwood number is based on D_b. Using this information, along with Eq. (17), the ratio of oxygen's permeability in blood to its permeability in water can be determined;

$$\frac{K_b}{K_w}=\left(\frac{D_b}{D_w}\right)^{2/3}\left(\frac{\nu_w}{\nu_b}\right)^{b-1/3}\left(1+\frac{c_T\lambda(\mathrm{PO_2})}{\alpha_b}\right)^{1/3}. \tag{19}$$

Figure 5 shows K_b/K_w plotted as a function of PO_2. In the numerical procedure, the permeability of oxygen in water is determined first, after which its permeability in blood is computed using Eq. (19).

Numerical Procedure

The improved Euler (predictor–corrector) method was used to solve Eq. (1)–(6) numerically in MATLAB. The PO_2 at time zero in each compartment was set at 40 mm Hg for blood (to reflect venous saturation levels), or

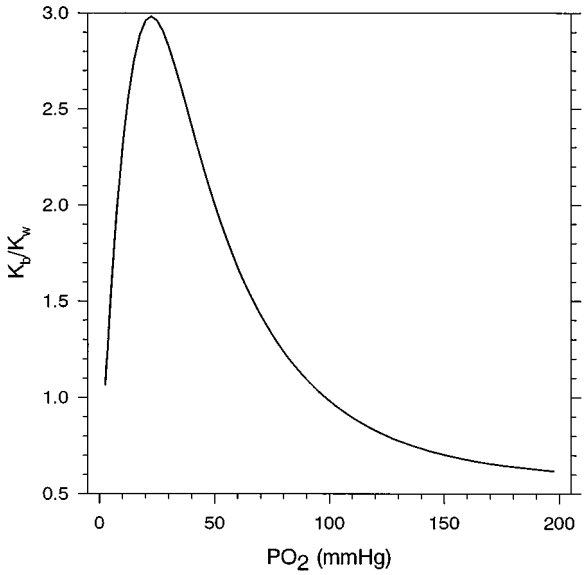

FIGURE 5. Ratio of oxygen's permeability in bovine blood to its permeability in water as a function of PO_2.

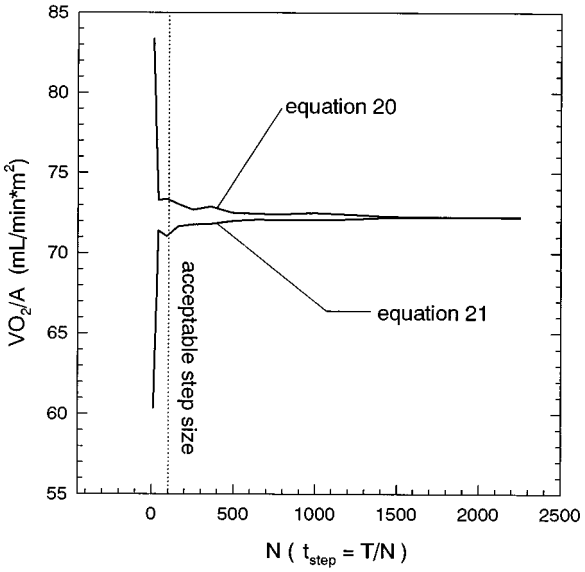

FIGURE 6. Convergence of the mass transfer rates calculated from Eq. (20) and (21) with decreasing step size. This simulation is for water, and results are normalized to the surface area of the device. Step size is shown as *N*, where 1/*N* is the fraction of the period (i.e., for $T=0.4$ s and $N=100$, $t_{step}=0.004$ s).

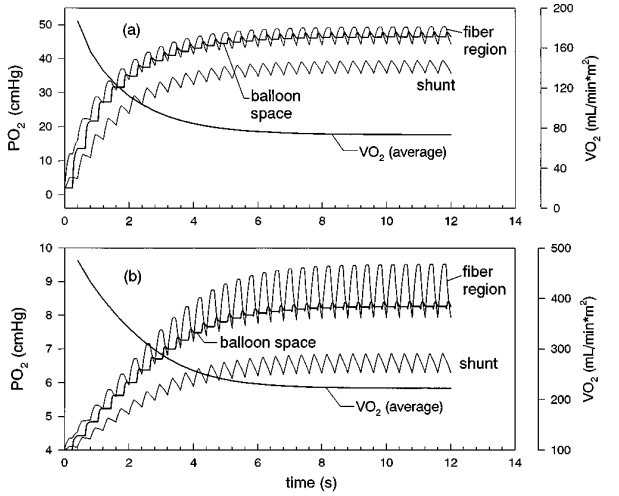

FIGURE 7. Typical simulation runs for (a) water and (b) blood. Simulation parameters are: $d_{hmf}=300\ \mu$m, $d_{b0}=1.5$ cm, $d_F=2.0$ cm, $L=40$ cm, $T_I=150$ ms, $d_T=2.5$ cm, $\epsilon=0.35$, $f=150$ bpm, $Q_L=3$ L/min and inlet PO_2's are 2 cm Hg for water and 4 cm Hg for blood. The surface area for this device is 4700 cm^2. These values correspond to a full-scale device, and are used in all subsequent simulations, except as otherwise stated.

20 mm Hg for water (to reflect our *in vitro* test conditions), and the simulations were run until the $PO_2(t)$ profiles in each compartment converged to steady-state oscillations. In implementing this procedure, it was necessary to include a small residual volume ($V_{res}\approx 0.05V_0$) in the balloon space region to ensure that the balloon space volume never goes exactly to zero. If the balloon space volume is exactly zero, a division by zero occurs in the governing Eqs. (5) and (6), which results in computational errors.

Once the $PO_2(t)$ in each compartment is known, it is possible to compute the mass transfer rate averaged over an oscillation cycle. An equation for the average mass transfer rate, $\overline{\dot{V}_{O_2}}(t)$, can be derived from the relation $\dot{V}_{O_2}=KA\Delta P$:

$$\overline{\dot{V}_{O_2}}(t)=\frac{1}{T}\int_t^{t+T} K(\tau)A\{\overline{P_{if}}-P_F(\tau)\}d\tau. \qquad (20)$$

The overall exchange rate can also be computed from a mass balance across the shunt region, yielding

$$\overline{\dot{V}_{O_2}}(t)=\frac{Q_L}{T}\int_t^{t+T}\{P_s(\tau)\alpha_s(\tau)-P_{in}\alpha_{in}\}d\tau, \qquad (21)$$

where $\alpha_s(t)$ is $\alpha_s(P_s(t))$ and α_{in} is $\alpha(P_{in})$; i.e., the effective solubilities computed using $P_s(t)$ and P_{in}. Figure 6 shows the convergence of these two mass transfer rates with decreasing step size for a typical water simulation. A step size of 1% of the period was chosen as an appropriate tradeoff between computation time (which is longer for smaller step sizes) and degree of convergence, since the $\overline{\dot{V}_{O_2}}(t)$ values differ by less than 5% at this point. The mass transfer rate in all subsequently described simulations was calculated using the relation between the partial PO_2 difference, permeability, and transfer rate [Eq. (20)]. The use of this equation instead of the mass balance across the shunt region [Eq. (21)] is arbitrary.

RESULTS AND DISCUSSION

PO_2 Dynamics

Typical simulations are presented in Figs. 7(a) (water) and 7(b) (blood) for impulsive inflation of the balloon. Shown are the PO_2 compartment values (left ordinate) and the period-averaged mass transfer rate normalized to the fiber surface area, $\overline{\dot{V}_{O_2}}(t)/A$ (right ordinate). The PO_2 in the fiber region increases with time until reaching steady state, and is greater than that within the shunt volume at all times $[P_F(t)>P_s(t)]$ for both water and blood. The buildup in the fiber region PO_2 leads to a decrement in mass transfer, as shown by the average mass transfer rate versus the time curve. For instance, $\overline{\dot{V}_{O_2}}(t)/A$ for water decreases 60% over the course of the

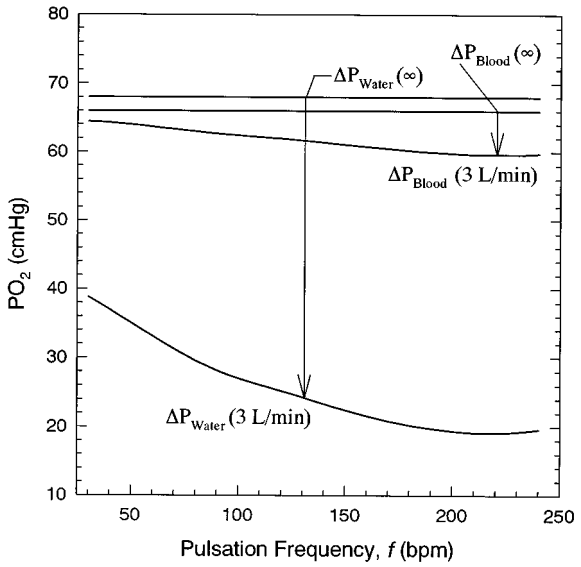

FIGURE 8. The driving force for transfer vs balloon pulsation frequency for water and blood, for a longitudinal flow rate of 3 L/min, and for an infinite longitudinal flow rate.

simulation, from 187 to 74 mL min^{-1} m^{-2}, and that for blood decreases 53%, from 475 to 222 mL min^{-1} m^{-2}.

The decrement in mass transfer is of about the same magnitude for both water and blood, yet the mechanism effecting these decrements is very different. Figure 8 demonstrates how the driving force for mass transfer, $\Delta P = P_{if} - P_F(t)$, averaged over one period changes with frequency for both fluids. The maximum possible (theoretical) mass transfer driving force, $\Delta P(\infty) = P_{if} - P_{inlet}$, is shown for reference. The $\Delta P(\infty)$ limit can only be reached as both frequency and longitudinal liquid flow rate approach infinity, thus providing the IMO with perfect mixing between the shunt and fiber regions, and with fresh (unoxygenated) fluid being delivered instantaneously, eliminating the PO_2 buildup. Conversely, the PO_2 difference decreases with increasing frequency over the range shown. While increasing the balloon pulsation frequency increases the driving force for transfer by ''quenching'' the fiber region with fresh fluid, it also augments the transverse velocity of fluid relative to the fibers, thereby increasing the amount of oxygen transferred into the fluid (by increasing the permeability) within the fiber region. Therefore, the ΔP versus frequency curve, for both fluids, is determined by two mutually opposed effects. In the limit, as both frequency and longitudinal flow rate approach infinity, however, the trend will be to maximize the driving force for transfer. As the hypothetical limit of infinite frequency is approached, the zone of oversaturated fluid in the fiber region will disappear [i.e., $P_s(t) \rightarrow P_F(t)$]. Further, when the longitudinal flow rate is infinite, the residence time of a fluid particle in the IMO will be zero, so there will not be time for oxygen transfer from the fibers to the fluid particle.

Figure 8 indicates that the driving force for transfer in blood is only slightly lower than its maximum possible value, whereas that for water is significantly below its maximum. The decrease in gas exchange shown in Fig. 7(a) (water) results entirely from the decrease in ΔP associated with the intrafiber region PO_2 buildup [see Eq. (16)]. Conversely, the gas exchange rate decreases significantly in blood without much decrease in the driving force for transfer. This is because the permeability K is very sensitive to PO_2 in blood. As the PO_2 increases from 40 mm Hg (typical venous inlet) to 100 mm Hg, the permeability of oxygen in blood decreases by almost 60% due to the saturation of hemoglobin (see Fig. 5). While the decrements in gas exchange are mediated by different phenomena in water and blood, the magnitude of the decrease is fortuitously about the same.

This analysis suggests that extrapolating gas exchange results from *in vitro* water experiments to *in vivo* blood experiments may be relatively straightforward. Consider the ratio of $\dot{V}_{O_2}$ in blood to that in water for a given IMO device and frequency of pulsation: $\dot{V}_{O_2}(b)/\dot{V}_{O_2}(w) \sim K_b \Delta P_b / K_w \Delta P_w$. For cases where there is not much of a buildup in the fiber-region PO_2 in water, $\Delta P_b \approx \Delta P_w$, so this ratio is just K_b/K_w. As shown in Fig. 5, this ratio is dependent on the blood PO_2, but is about 1.9 when averaged from 40 mm Hg (venous inlet) to 80 mm Hg (arterial outlet), and so a given device will transfer about twice as much O_2 in blood as in water. In water, however, the fiber-region PO_2 may increase significantly, approaching the intrafiber levels and subsequently decreasing the IMO's mass transfer efficiency. This effect will not be nearly as pronounced for a device tested in blood (so, $\Delta P_b > \Delta P_w$), but even a slight increase in fiber-region blood PO_2 will facilitate a decrement in mass transfer by leading to a decreased permeability in that region. In effect, the zone of oversaturated water is replaced by a zone of oversaturated hemoglobin. For instance, Fig. 5 shows that the ratio K_b/K_w averaged between 40 and 120 mm Hg is about 1.4. Thus, the increase in $\Delta P_b/\Delta P_w$ is counterbalanced by the decrease in K_b/K_w, and $\dot{V}_{O_2}(b)/\dot{V}_{O_2}(w)$ is still about 2 (e.g., $\Delta P_b/\Delta P_w \approx 2/1.4$). This is relatively consistent with our previous experiments,[4] which show that mass transfer rates in blood are greater than those in water by a factor ranging from 2 to 3.

Mode of Balloon Pulsation

Figure 9 compares impulsive and sinusoidal oscillation modes in water (a) and blood (b). At the lower frequencies, sinusoidal inflation is 40%–50% better than impulsive inflation. For instance, at 30 bpm in blood,

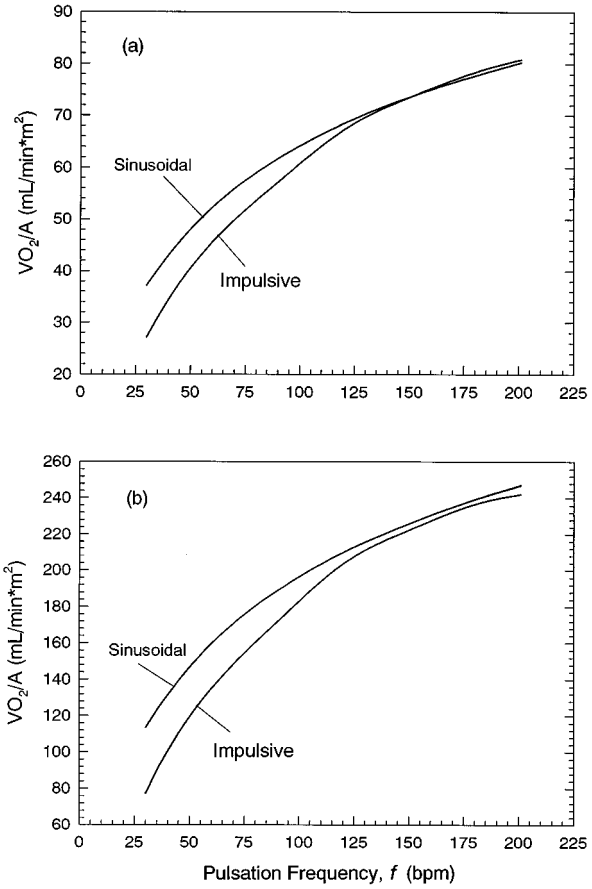

FIGURE 9. Average mass transfer rate [$\dot{\overline{V}}_{O_2}(t)/A$] vs frequency for sinusoidal and impulsive inflation modes, in (a) water and (b) blood.

impulsive inflation will result in an oxygen transfer rate, $\dot{\overline{V}}_{O_2}(t)/A$, of about 80 mL min^{-1} m^{-2}, whereas sinusoidal inflation will yield about 115 mL min^{-1} m^{-2}. Consider a balloon pulsating in the impulsive mode at 30 bpm, for which the period of an inflation–deflation wave form is 2s. At this frequency, the balloon will inflate completely in the first 0.15 s, remain inflated and motionless for the next 1.7 s, then deflate in the last 0.15 s. Thus, 85% of every period is a dead time during which there is no balloon motion and thus no convectively driven oxygen transfer. While the 0.15 s periods of rapid balloon inflation and deflation are associated with high mass transfer rates, they cannot compensate for the dead time during which there is no transfer, and so the continual sinusoidal wave form leads to better mass transfer. When the period is exactly twice the inflation time ($f = 0.5 \times T_I^{-1}$), the impulsive inflation wave form will become a triangular wave [see Fig. 3(b)], which is virtually indistinguishable from a sine wave in terms of mass transfer performance. This explains the convergence of the mass transfer rates at higher frequencies. For a prototype impulsively filling and emptying with a 0.15 s inflation time, the maximum effective frequency of pulsation is 200 bpm (3 1/3 Hz). Above this frequency, mass transfer will plateau since the balloon does not have enough time to fill and empty completely (in Fig. 9, the sinusoidal mode was also limited to 200 bpm).

This analysis has important implications for design of the IMO's drive system. While sinusoidal inflation is superior at low frequencies ($<\approx$90–100 bpm), the target frequency range for IMO balloon pulsation *in vivo* is above 100 bpm. In principle, the highest possible pulsation frequency is desirable, since more rapid balloon pulsation is associated with higher mass transfer rates. *In vivo* placement, however, will probably impose an upper limit of 180–200 bpm, since adding too much pulsatility to the venous flow may adversely affect venous return, and too much agitation of the blood could lead to red blood cell damage. Within this range, there is essentially no difference between sinusoidal and impulsive oscillation modes. The effort required to build a drive system based on sinusoidal oscillation (such as a piston–crankshaft-type mechanism) may therefore be unjustified, since pneumatic systems containing solenoid-actuated valves (such as the Datascope Intra-Aortic Balloon Pump console) tend to be simpler and more reliable.

Comparison of Experiment and Theory

Figure 10 compares the theoretical and actual mass transfer rates for two existing prototypes in water at 37 °C, over a range of balloon pulsation frequencies. These prototypes were tested as previously described[4] with an *in vitro* characterization apparatus. The principal elements of this apparatus are a 2.54 cm internal diameter Plexiglas tube into which the prototype is placed (cava test section), compliance chambers for absorbing the balloon-generated flow, deoxygenators and heat exchangers, and a Biomedicus pump. The oxygen partial pressure in the cava test section is measured before and after the device, and used to compute the oxygen exchange rate. Experimental results are shown as balloon-engendered gas transfer rates, $\dot{\overline{V}}_{O_2}(t)_f - \dot{\overline{V}}_{O_2\ 0bpm}$. The theoretical predictions correlate closely with experimental results, and the deviations between experiment and theory above about 120 bpm arise from simplifications in modeling the balloon pulsation dynamics. While the model assumes a constant rate of inflation, the actual rate of inflation decreases at higher beat rates due to inertial effects and the limitations of the drive system.

Optimal Balloon Size

Optimization of IMO device geometry and operation is a key application of this design model. The geometric and operational parameters which need to be selected

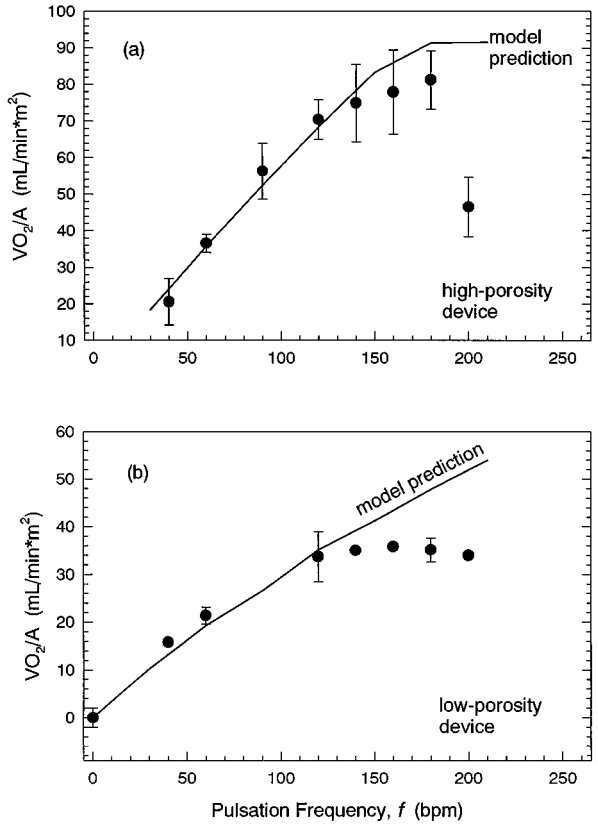

FIGURE 10. Actual and theoretical mass transfer results for (a) the D14 prototype and (b) the D15 prototype. The actual results are from *in vitro* testing in water, and mass transfer rates are normalized to the device surface area. D14 is an 18.5 cm long, high-porosity device ($\epsilon \approx 0.7$) with 380 μm outer diameter (OD) fibers, an overall diameter (d_F) of about 2 cm, a balloon size (V_0) of 30 mL ($d_{b0} \approx 1.4$ cm), and a total surface area of 850 cm^2. D15 is a low-porosity device ($\epsilon \approx 0.4$) 19 cm in length, with 400 μm OD fibers, a 10 mL balloon ($d_{b0} \approx 0.8$ cm) and 1895 cm^2 of fiber surface area. Both devices were tested in a rigid, Plexiglas tube with an internal diameter (d_T) of 2.5 cm, and a longitudinal liquid flow rate, Q_L, of 3 L/min.

include fiber bundle porosity ϵ and length L, the frequency of balloon pulsation, f, balloon diameter d_{b0} and inflation time T_I, overall device diameter d_F, and fiber diameter d_{hmf}. Formal optimizations are not required in selecting most of these parameters. A decrease in porosity ϵ (increase in fiber-packing density) will facilitate higher transverse velocities by forcing the fluid to accelerate (and ''squeeze'') between more closely packed fibers, thereby increasing mass transfer efficiency. A low-porosity device will also have more fibers, so decreasing porosity has a double advantage for mass transfer. Device surface area can also be augmented by increasing length, increasing diameter, and/or decreasing the fiber size (and thus increasing the total number of fibers). Similarly, increasing the balloon pulsation frequency will increase mass transfer efficiency. The inflation time parameter is a more complex issue since it involves characteristics of the drive system as well as device geometry, but in general, a shorter inflation time would be better since shorter inflation times will allow for complete balloon filling and emptying at higher pulsation rates. Ultimately, the frequency of balloon pulsation will be dictated by the mechanical limits of the drive system and the fragility of red blood cells (such issues are beyond the scope of the present analysis). Thus, six of these seven parameters will ultimately be selected by constraints rather than optimizations, but the device performance can be optimized with respect to the balloon diameter. For instance, small balloons are associated with low mass transfer rates, because they provide little active mixing. Conversely, large balloons take away from the space available for fibers since the vena cava is limited in size.

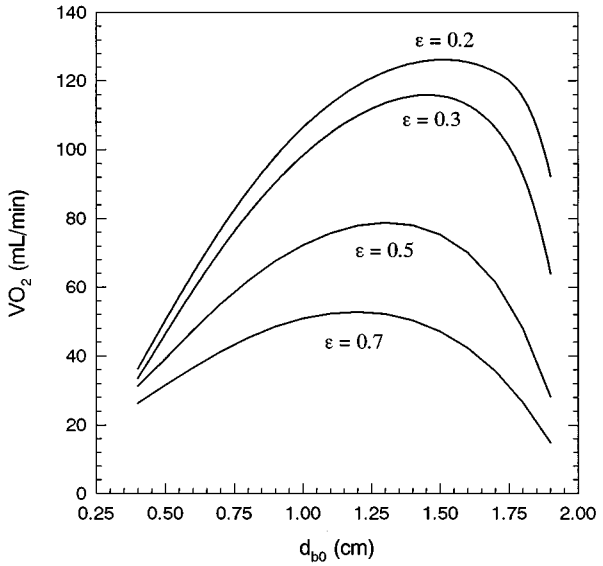

FIGURE 11. Average mass transfer rate [$\dot{V}_{O_2}(t)$] in blood vs balloon diameter.

Figure 11 shows the mass transfer rate in blood, $\overline{\dot{V}_{O_2}(t)}$, as a function of balloon size for different porosity devices. A balloon diameter of about 1.5 cm, which corresponds to 71 mL for a 40 cm length balloon, will maximize mass transfer performance. This value, however, depends slightly on fiber bundle porosity. High-porosity devices require more volume to fit a given number of fibers, and this detracts from the space available for the balloon. Furthermore, the mass transfer efficiency is dependent on device porosity, so different devices will require a different number of fibers to achieve a given level of mass transfer. Despite these variations, the model suggests that a 1.5 cm balloon will lead to optimal or near-optimal mass transfer performance in the IMO in the porosity range of interest (0.2–0.7). This is close to

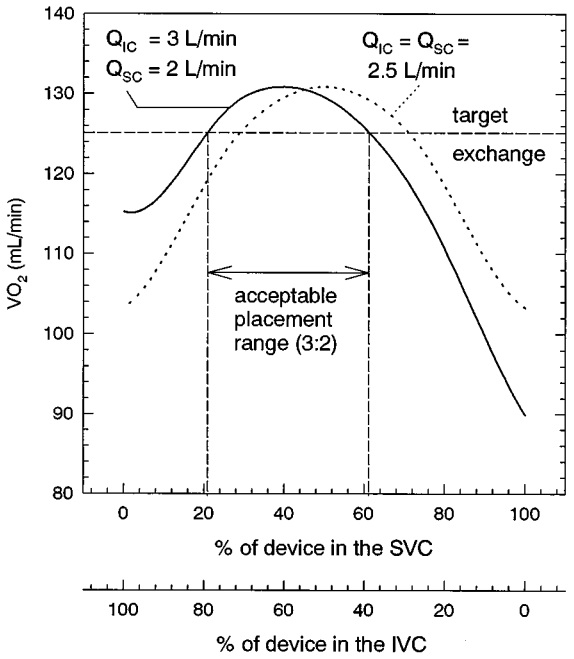

FIGURE 12. Effect of device placement within the IVC/SVC on mass transfer (in blood) for two different flow rates in the IVC and SVC.

the size of the balloons currently used in IMO prototypes, which are about 1.3–1.5 cm in diameter.

Implications of Intravascular Placement

Figure 12 illustrates the effect of intravascular positioning on the total mass transfer rate $[\dot{\overline{V}}_{O_2}(t)]$. The x axis gives the relative distribution of the device within the inferior and superior vena cavae (IVC and SVC) for a 40 cm length IMO. The two curves are for two different flow rate partitionings between the IVC and SVC; the left (solid) curve represents a 3:2 division and the right (dashed curve) shows a 2.5:2.5 division (the total cardiac output is 5 L/min for both cases). These results were obtained by modeling the IVC and SVC as two noninteracting vessels in parallel that empty into a common vessel [the right atrium (RA)], with the same inlet PO_2 of 40 mm Hg, and flow rates of Q_{IC} and Q_{SC}, respectively. The IMO is treated as two separate devices of exactly the same cross section, but with different lengths. Since the total length of the IMO is 40 cm, the length of device 1 plus device 2 is 40 cm. Thus, a device partitioning of 60% in the IVC and 40% in the SVC was approximated by a 24 cm device in the IVC and a 16 cm device in the SVC. Since the IVC and SVC are treated as separate, parallel vessels which have no interaction except that they empty into a common outlet (RA), the results will slightly overemphasize the effect of intravascular placement (since, *in vivo*, there will be some mixing of IVC and SVC blood associated with balloon movement). Incorporating a mixing effect, however, would substantially increase the complexity of the model.

The optimal gas exchange rate for both flow rate situations is about 131 mL/min (our design goal is 125 mL/min), but the optimal placement for the 2.5:2.5 flow rate is 50% in each vessel, whereas that for the 3:2 IVC:SVC flow partitioning (which is about what we expect *in vivo*) is 60% in the IVC and 40% in the SVC. In other words, if 60% of the cardiac output is going through the IVC, then 60% of the device should be placed in the IVC, and if 50% of the output is going through the IVC, then 50% of the device should be placed there, etc. Another important issue that can be addressed with this analysis is the loss of gas exchange performance associated with nonoptimal placement. Figure 12 shows that a 40 cm IMO should be able to transfer at least the target level of gas exchange even if it is not optimally placed. For instance, while optimal exchange occurs when 60% of the device is in the IVC, placing anywhere between 40% and 80% of the device in the IVC will still yield gas exchange at or above the target level. This is particularly important, since the *in vivo* placement ratio (% of IMO in IVC: % in SVC) will probably not be selectable, but rather dictated by the geometry of the venous system. We expect that the entire length of the IVC plus SVC will be about equivalent to the IMO length (40 cm), so that the IMO will not be movable once in place (movement could obstruct venous return through the smaller vessels), and the placement ratio will simply be IVC length: SVC length. Ultimately, this analysis reveals that, while mass transfer can be somewhat enhanced by device repositioning, the target level of gas exchange should still be attainable even if the IMO is not optimally placed. As the model is further refined, the impact of other aspects of venous anatomy such as vessel diameter and compliance could be used to give more accurate estimates of *in vivo* gas exchange performance in different patients.

ACKNOWLEDGMENTS

This work was supported by the United States Army Medical Research, Development, Acquisition and Logistics Command under Contract No. DAMD 17-94-C-4052. The views, opinions and/or findings contained in this report are those of the authors and should not be construed as an official Department of the Army position, policy, or decision unless so designated by other documentation. This work has also been supported by Medtronic, Inc. Funding for the graduate education of the principal author was provided by a Special Opportu-

nity Award from the Whitaker Foundation. The authors thank Mariah Hout for her contributions to the experiments discussed in this paper.

REFERENCES

[1] Ahmed, T., and M. J. Semmens. Use of transverse flow hollow fibers for bubbleless membrane aeration. *Water Res.* 30:440–446, 1996.
[2] Conrad, S. A., *et al.* Major findings from the clinical trials of the intravascular oxygenator. *Artif. Organs* 18:846–863, 1994.
[3] Fazzalari, F. L., R. H. Bartlett, M. R. Bonnell, and J. P. Montoya. An intrapleural lung prosthesis: Rationale, design, and testing. *Artif. Organs* 18:801–805, 1994.
[4] Federspiel, W. J., T., Hewitt, M. S. Hout, F. R. Walters, L. W. Lund, P. I. Sawzik, G. Reeder, H. S. Borovetz, and B. G. Hattler. Recent progress in engineering the Pittsburgh intravenous membrane oxygenator. *ASAIO J.* 42:M435–M442, 1996.
[5] Fujii, Y., and S. Kigoshi. Characterization of hollow fiber membranes. *J. Chem. En. J.* 27:321–328, 1994.
[6] Gattinoni, L., A. Pesenti, and G. P. Rossi. Treatment of acute respiratory failure with low-frequency positive-pressure ventilation and extracorporeal removal of CO_2. *Lancet* 2:292–294, 1980.
[7] Ichiba, S., and R. H. Bartlett. Current status of extracorporeal membrane oxygenation for severe respiratory failure. *Artif. Organs* 20:120–123, 1996.
[8] Incropera, F. P., and D. P. DeWitt. Introduction to Heat Transfer. New York: Wiley, 1990.
[9] Lund, L. W. Evaluation of flow visualization methods as a design tool for artificial lung development. Carnegie Mellon University, Masters thesis, 1992.
[10] Macha, M., W. J., Federspiel, L. W. Lund, P. J. Sawzik, P. Litwak, F. P. Walters, G. D. Reeder, H. S. Borovetz, and B. G. Hattler. Acute *in vivo* studies of the Pittsburgh intravenous membrane oxygenator. *ASAIO J.* 42:M609–M615, 1996.
[11] Makarewicz, A. J. Static and dynamic artificial lungs. Ph.D. thesis, Northwestern University, 1994.
[12] Mockros, L. F., and R. Leonard. Compact cross-flow tubular oxygenators. *Trans. Am. Soc. Artif. Intern. Organs* 31:628–632, 1985.
[13] Mortensen, J. D. Intravascular oxygenator: A new alternative method for augmenting blood gas transfer in patients with acute respiratory failure. *Artif. Organs* 16:75–82, 1992.
[14] Niranjan, S. C., J. W. Clark, K. Y. San, J. B. Zwischenberger, and A. Bidani. Analysis of factors affecting gas exchange in intravascular blood gas exchanger. *J. Appl. Physiol.* 77:1716–1730, 1994.
[15] Pesenti, A., L. Gattinoni, T. Kobolow, and G. Damia. Extracorporeal circulation in adult respiratory failure. *ASAIO Trans.* 34:43–47, 1988.
[16] Snider, M. T., D. B. Campbell, W. A. Kofke, K. M. High, G. B. Russell, M. F. Keamy, and D. R. Williams. Venovenous perfusion of adult and children with severe acute respiratory distress syndrome. *ASAIO Trans.* 34:1014–1020, 1988.
[17] Vaslef, S. N., K. E. Cook, R. J. Leonard, L. F. Mockros, and R. W. Anderson. Design and evaluation of a new, low pressure loss, implantable artificial lung. *ASAIO J.* 40:M522–M526, 1994.
[18] Vaslef, S. N., R. W. Anderson, and R. J. Leonard. Use of a mathematical model to predict oxygen transfer rates in hollow fiber membrane oxygenators. *ASAIO J.* 40:990–996, 1994.
[19] Weinberger, S. E. Principles of Pulmonary Medicine. Philadelphia: Saunders, 1992.
[20] Wickramasinghe, S. R., M. J. Semmens, and E. L. Cussler. Mass transfer in various hollow fiber geometries. *J. Membr. Sci.* 69:235–250, 1992.
[21] Yang, M. C., and E. L. Cussler. Designing hollow fiber contactors. *AIChE. J.* 32:1910–1916 1986.